Noninvasive imaging of immune responses

Mohammad Rashidian[a,b,1], Edmund J. Keliher[c,d,1], Angelina M. Bilate[a], Joao N. Duarte[a], Gregory R. Wojtkiewicz[c], Johanne Tracey Jacobsen[a,e], Juanjo Cragnolini[a], Lee Kim Swee[a], Gabriel D. Victora[a], Ralph Weissleder[c,d,f], and Hidde L. Ploegh[a,b,2]

[a]Whitehead Institute for Biomedical Research, Cambridge, MA 02142; [b]Department of Biology, Massachusetts Institute of Technology, Cambridge, MA 02142; [c]Center for Systems Biology, Massachusetts General Hospital, Boston, MA 02114; [d]Department of Radiology, Massachusetts General Hospital, Boston, MA 02114; [e]Center for Immune Regulation, Oslo University Hospital, University of Oslo, N-0372 Oslo, Norway; and [f]Department of Systems Biology, Harvard Medical School, Boston, MA 02115

Edited by Owen N. Witte, Howard Hughes Medical Institute, University of California, Los Angeles, CA, and approved March 17, 2015 (received for review February 18, 2015)

At their margins, tumors often contain neutrophils, dendritic cells, and activated macrophages, which express class II MHC and CD11b products. The interplay between stromal cells, tumor cells, and migratory cells such as lymphocytes creates opportunities for noninvasive imaging of immune responses. We developed alpaca-derived antibody fragments specific for mouse class II MHC and CD11b products, expressed on the surface of a variety of myeloid cells. We validated these reagents by flow cytometry and two-photon microscopy to obtain images at cellular resolution. To enable noninvasive imaging of the targeted cell populations, we developed a method to site-specifically label VHHs [the variable domain (V_H) of a camelid heavy-chain only antibody] with ^{18}F or ^{64}Cu. Radiolabeled VHHs rapidly cleared the circulation ($t_{1/2} \approx$ 20 min) and clearly visualized lymphoid organs. We used VHHs to explore the possibility of imaging inflammation in both xenogeneic and syngeneic tumor models, which resulted in detection of tumors with remarkable specificity. We also imaged the infiltration of myeloid cells upon injection of complete Freund's adjuvant. Both anti-class II MHC and anti-CD11b VHHs detected inflammation with excellent specificity. Given the ease of manufacture and labeling of VHHs, we believe that this method could transform the manner in which antitumor responses and/or infectious events may be tracked.

PET imaging | non-invasive imaging | inflammation | cancer | camelid single domain antibodies

Myeloid cells, such as neutrophils, dendritic cells, and activated macrophages, express CD11b and/or class II MHC products and are often present at the tumor margin (1, 2). Macrophages, depending on their functional properties (M1 or M2 type) (3), help establish a (micro) environment either detrimental or favorable to tumor growth (3, 4). The ability to image myeloid cells' presence is thus of diagnostic relevance and may be an approach more generally applicable than detection of tumor cells via unique tumor-specific markers. Current practice either relies on sampling of peripheral blood to enumerate and characterize these cells in the circulation or requires more invasive procedures, such as histological analysis of biopsies or surgical resection specimens. Noninvasive detection of sites of an ongoing inflammatory or immune response might provide clues to the existence and location of tumor foci, which a biopsy could then confirm. PET tracers, such as ^{18}F-2-deoxyfluoroglucose (FDG), visualize differences in metabolic activity that accompany inflammation but lack the discriminatory power that antibodies or their fragments might afford (5). To detect inflammatory cells by recognition of surface markers, we developed imaging tools to track the behavior of class II MHC$^+$ and CD11b$^+$ cells in mice.

Several obstacles stand in the way of using full-sized antibodies for in vivo imaging. First, installation of an appropriate fluorescent or radioactive label onto the relevant antibodies without inflicting damage to the antibody itself is at times demanding. Second, the short half-lives of isotopes most suitable for PET imaging (^{18}F, $t_{1/2}$ = 110 min; ^{68}Ga, $t_{1/2}$ = 68 min; ^{64}Cu, $t_{1/2}$ = 12 h) require rapid generation and purification of the desired adduct, which is often impractical. Third, tissue penetration of a full-sized antibody is poor. Finally, a labeled, full-sized antibody persists in the circulation because of its comparatively long circulatory half-life. Other scaffolds, such as proteins based on fibronectin type III domains (FN3) and small molecules that serve as receptor-specific ligands, have also been used for PET imaging (6, 7) but do not provide information about immune responses (6, 7). Camelid-derived single-domain VHHs [the variable domain (VH) of a camelid heavy-chain only antibody] (8) present several advantages and workarounds that address these obstacles. VHHs are smaller (~15 kDa) than immunoglobulins (~150 kDa), "diabody" antibody derivatives (~60 kDa) (9), Fab fragments (~50 kDa), or ScFvs (~25 kDa), and they lack an Fc region. Single-domain VHHs of desired specificity can be readily generated, isolated, and characterized by their amino acid sequence using standard procedures (10). Approaches to modify (11) and humanize (12) these camelid VHHs exist, and early-phase clinical testing is underway (13).

Results

Anti-Mouse Mouse Class II MHC and Anti-Mouse CD11b Stain Secondary Lymphoid Organs. Two VHHs, VHH7 (anti-mouse class II MHC) and VHHDC13 (anti-mouse CD11b) were generated following standard procedures (*SI Materials and Methods*) (10). To test whether anti-class II MHC and anti-CD11b–specific VHHs could be used for in vivo labeling of class II MHC- and CD11b-expressing cells, we installed a fluorophore on VHH7 and

Significance

Tumors are often surrounded and invaded by bone marrow-derived cells. Imaging the infiltration of such immune cells into tumors may therefore be an attractive means of detecting tumors or of tracking the response to anticancer therapy. We show that it is possible to detect these cells noninvasively by positron emission tomography (PET) via the surface markers displayed by them. The ability to monitor the immune response in the course of therapy will enable early determination of the efficacy of treatment and will inform decisions as to whether treatment should be stopped or continued. Noninvasive monitoring could therefore change how therapies are applied and assessed, to the benefit of many patients.

Author contributions: M.R., E.J.K., A.M.B., and H.L.P. designed research; M.R. synthesized the substrates, expressed sortase and VHHs, and modified VHHs with fluorophores and for ^{64}Cu/^{18}F labeling; E.J.K. performed synthesis of ^{18}F/^{64}Cu-labeled VHH and their characterizations; M.R., E.J.K., G.R.W., and R.W. performed PET-CT imaging and analysis of the PET-CT data; M.R., A.M.B., J.T.J., and G.D.V. performed and interpreted two-photon microscopy; M.R., A.M.B., and J.N.D. performed FACS experiments; J.N.D., J.C., and L.K.S. identified VHH7 and DC13; and M.R. and H.L.P. wrote the paper.

The authors declare no conflict of interest.

This article is a PNAS Direct Submission.

See Commentary on page 5868.

[1] M.R. and E.J.K. contributed equally to this work.

[2] To whom correspondence should be addressed. Email: ploegh@wi.mit.edu.

This article contains supporting information online at www.pnas.org/lookup/suppl/doi:10.1073/pnas.1502609112/-/DCSupplemental.

www.pnas.org/cgi/doi/10.1073/pnas.1502609112

VHHDC13 in a sortase-catalyzed reaction and used this preparation for two-photon microscopy and flow cytometry (14). We have previously established that VHH7 recognizes murine I-A products encoded by the H-2^b haplotype and that VHH7 fails to stain class II MHC$^{-/-}$ cells (11). VHH7 does not recognize human class II MHC products, as ascertained by immunofluorescence on class II HLA$^+$ Mel-Juso cells maintained in culture. We injected 20 μg of Texas Red-labeled VHH7 i.v. into class II MHC-eGFP (15) or class II MHC-deficient mice (16). After 90 min, we explanted lymph nodes and spleen to subject them to two-photon microscopy. The class II MHC-eGFP marker enables visualization of all class II MHC$^+$ cells without the aid of an antibody, and therefore the efficacy of in vivo immunostaining with VHH7 can be accurately assessed. Two-photon imaging of class II MHC-eGFP mice showed perfect concordance with Texas Red-VHH7–stained cells (Fig. 1 *A* and *B*). Class II MHC$^{-/-}$ mice showed no specific staining (Fig. 1*C*). In the absence of injected Texas Red-VHH7, no staining was apparent in the corresponding channel (Fig. 1*A* and Fig. S1). These results establish specificity of staining and show that, at 90 min postinjection, VHH7 achieved excellent penetration of spleen and lymph nodes. We similarly labeled VHHDC13, which recognizes CD11b, a marker for neutrophils, macrophages, and dendritic cells. The molecular target of VHHDC13 was identified by mass spectrometry of immunoprecipitates prepared with immobilized VHHDC13. VHHDC13 specifically binds to CD11b$^+$ cells in lymph nodes and spleen (Fig. 1 *E1* and *E2* and Fig. S1). To further confirm the two-photon experiments, WT, MHC-II–deficient, or CD11b-deficient mice were injected with 2 or 20 μg of VHH7 or VHHDC13-Alexa 647. After 90 min, spleen and brachial lymph nodes were analyzed by flow cytometry after staining with fluorophore-conjugated antibodies to CD3 and CD19, for VHH7, and to CD11b, for DC13. Results clearly confirmed the specificity of the VHHs for their corresponding targets (Fig. 1 *G* and *H*). In vivo staining with labeled VHHs obviates the need for fluorescent-protein fusions as the target for multiphoton imaging. A 90-min delay between administration and imaging is sufficient to obtain adequate staining with VHHs in spleen and lymph nodes. Although two-photon microscopy affords cellular resolution and can be used intravitally, it is nonetheless a mostly invasive method. We therefore explored the possibility of noninvasive imaging by positron emission tomography (PET).

Site-Specific ^{18}F or ^{64}Cu Labeling of Single-Domain Antibodies (VHHs) Using Sortase. Antibody-labeling strategies for PET often revolve around modification with metal chelators to enable installation of radioisotopes such as ^{64}Cu, ^{68}Ga, or ^{89}Zr (17–19). Although the

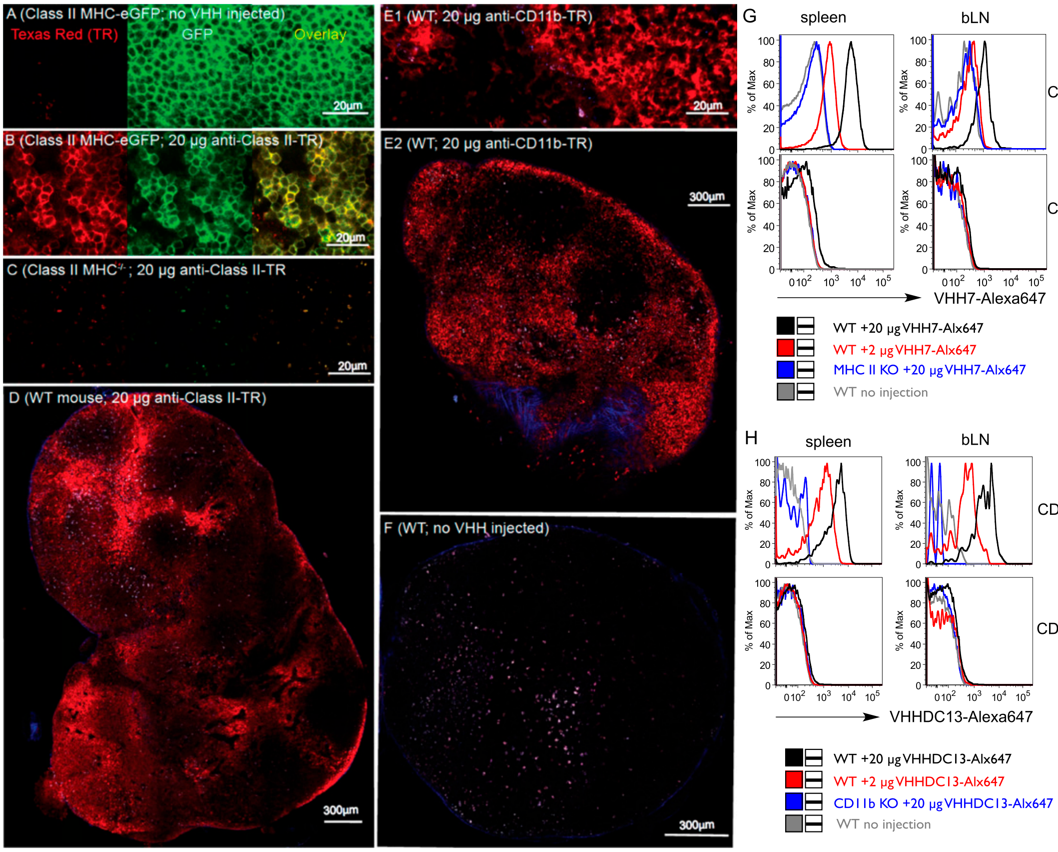

Fig. 1. VHH7 (anti-mouse class II MHC) and VHHDC13 (anti-mouse CD11b) stain secondary lymphoid organs. VHHs were site-specifically labeled with Texas Red or Alexa 647 via sortagging. In *A*–*F*, images were acquired using two-photon microscopy. In *A*, *B*, and *C*, the *Left* and *Middle* panels show the Texas Red and GFP channels, respectively. The *Right* panels are overlays. (*A*) Images of a lymph node of a class II MHC-eGFP knock-in mouse, no VHH injection prior to imaging. (*B*) Images of a lymph node of a class II MHC-eGFP knock-in mouse injected with 20 μg of VHH7-Texas Red 90 min prior to imaging. (*C*) Images of a lymph node of a class II MHC$^{-/-}$ mouse injected with 20 μg of VHH7-Texas Red 90 min prior to imaging. (*D*) Image of a lymph node of a B6 mouse injected with 20 μg of VHH7-Texas Red 90 min prior to imaging. (*E1* and *E2*) Image of a lymph node of a B6 mouse injected with 20 μg of VHHDC13-Texas Red 90 min prior to imaging. *E1* is a larger magnification of the lymph node shown in *E2*. (*F*) Image of a lymph node of a B6 mouse with no VHH injected. All injections were done intravenously. See Fig. S1 for images of spleen. See Images S1–S4 for high-resolution images of lymph nodes. (*G*) WT or class II MHC-deficient mice were injected or not with 2 or 20 μg of VHH7-Alexa 647. After 2 h, spleen and brachial lymph nodes (bLNs) were harvested, and cell suspensions were stained with anti-CD19 and anti-CD3 antibodies prior to FACS analysis. (*H*) WT or CD11b-deficient mice were injected or not with 2 or 20 μg of VHHDC13-Alexa 647. After 2 h, spleen and brachial lymph nodes (bLNs) were harvested, and cell suspensions were stained with anti-CD11b and anti-CD3 antibodies prior to FACS analysis. Histograms are representative of three to four mice with similar results.

creation of fluorine–carbon bonds remains a synthetic challenge (20, 21), its use has advantages over ^{68}Ga, ^{64}Cu, ^{89}Zr, and ^{124}I: lower energy positron emission, shorter half-life, reduced cost, and wider availability. ^{18}F-PET imaging is used both for diagnostic purposes and to monitor therapeutic efficacy, but these applications rely on agents that report on metabolic activity, such as FDG or labeled precursors to nucleic acids (22–25). The feasibility of noninvasive imaging of lymphocytes using an antibody fragment was demonstrated only recently, using an ∼60-kDa ^{64}Cu-labeled anti-CD8 antibody fragment (26). The half-life ($t_{1/2} \approx 110$ min) of ^{18}F requires it to be used shortly after installation. We therefore developed a simple two-step process (Fig. 2) for ^{18}F labeling of VHHs bearing a sortase-recognition motif, using a combination of a click reaction and a sortase-catalyzed modification. This method is robust, reproducible, and site-specific, without compromising the VHH antigen-binding site. This technique is further applicable to any other suitably modified biological entity (11).

The ^{18}F radionuclide was conjugated to the VHHs via a tetrazine (Tz)/transcyclooctene (TCO) reverse-electron demand Diels–Alder cycloaddition. The TCO–tetrazine reaction is the fastest known bioorthogonal reaction to date, with an estimated second-order rate constant of 210–26,000 $M^{-1} \cdot s^{-1}$ (27–29). We synthesized the requisite sortase nucleophile, GGG-tetrazine, which participates in sortase reactions to modify the VHH (Fig. 2*A*). ^{18}F radiolabeling of tosyl-transcyclooctene (TCO) was achieved with [^{18}F]-F/K222/K_2CO_3 in DMSO for ∼10 min at 90 °C to produce ^{18}F-TCO (30) (∼75% yield, decay-corrected) and purified by HPLC (Fig. 2*B*). ^{18}F-TCO was then added to the Tz-modified VHH, and the reaction was allowed to proceed for ∼20 min at pH 7. Thus, using ^{18}F-TCO, we readily produced >5 mCi of ^{18}F-labeled VHH7 in two steps (Fig. 2*C*). The ^{18}F-labeled VHH was purified by size-exclusion chromatography in PBS, providing a radiolabeled VHH solution ready for injection. Labeling experiments with ^{18}F-TCO yielded ^{18}F-VHH7 in 61 ± 9% decay-corrected radiochemical yield.

^{18}F-VHH7 Detects Secondary Lymphoid Organs. Administration of 200 μCi/10 μg ^{18}F-VHH7 in vivo in C57BL/6 WT mice (class II MHC-sufficient) allowed us to visualize lymph nodes, spleen, and thymus with a high degree of specificity and with excellent signal-to-noise ratios (Fig. 2 *G*–*J*). No nonspecific staining was seen in lymphoid tissues when using ^{18}F-VHH7 in class II MHC-II$^{-/-}$ mice (B6.129S2-H2 < dlAb1-Ea>/J) (Fig. 2 *F* and *K*–*M* and Movies S1*A*, S1*B*, S2*A*, and S2*B*). Biodistribution and circulatory half-life measurements of ^{18}F-VHHs in WT mice showed a $t_{1/2}$ of ∼20 min (Fig. S2).

^{18}F-VHH7 and ^{18}F-VHHDC13 Detect Inflammation. We next used ^{18}F-VHH7 and DC13 to image the behavior of class II MHC^{+} host cells in a xenograft tumor model. Neither the distribution of class II MHC^{+} or CD11b^{+} cells at steady state nor changes in their distribution and location over time have been specifically imaged noninvasively using ^{18}F-labeled tracers.

In many tumor models, the margins of the tumor contain macrophages, which, when activated, express class II MHC and CD11b (1, 3). Thus, we asked whether—in addition to the usual lymphoid structures as visualized by ^{18}F-VHH7 and DC13—we could detect the presence of macrophages around and within a xenografted tumor. We created xenografts in NOD-SCID mice by s.c. inoculation of the Mel-Juso human melanoma cell line, representative of a subset of human melanomas. The NOD-SCID hosts contain no B or T cells, but murine class II MHC^{+} antigen-presenting cells (macrophages and dendritic cells) and CD11b^{+} cells (macrophages, dendritic cells, and neutrophils) are present and should thus be visible by PET imaging with ^{18}F-VHH7 or DC13. One month after injection of 5×10^{6} tumor cells, PET imaging using ^{18}F-VHH7 (Fig. 3 *A*–*D*) or DC13 (Fig. 3 *F* and *G*) clearly showed the presence of class II^{+} cells or CD11b^{+} cells associated with the tumor (Movies S3 and S4). Some tumors, such as a subset of melanomas, express class II MHC products, in which case one might expect an even stronger PET signal (31). To confirm the presence of class II MHC^{+} cells or CD11b^{+} cells, we excised the tumors, digested them with collagenase D, and enriched tumor-infiltrating cells on Percoll gradients before flow cytometry. Mouse CD45^{+} tumor-infiltrating cells stained

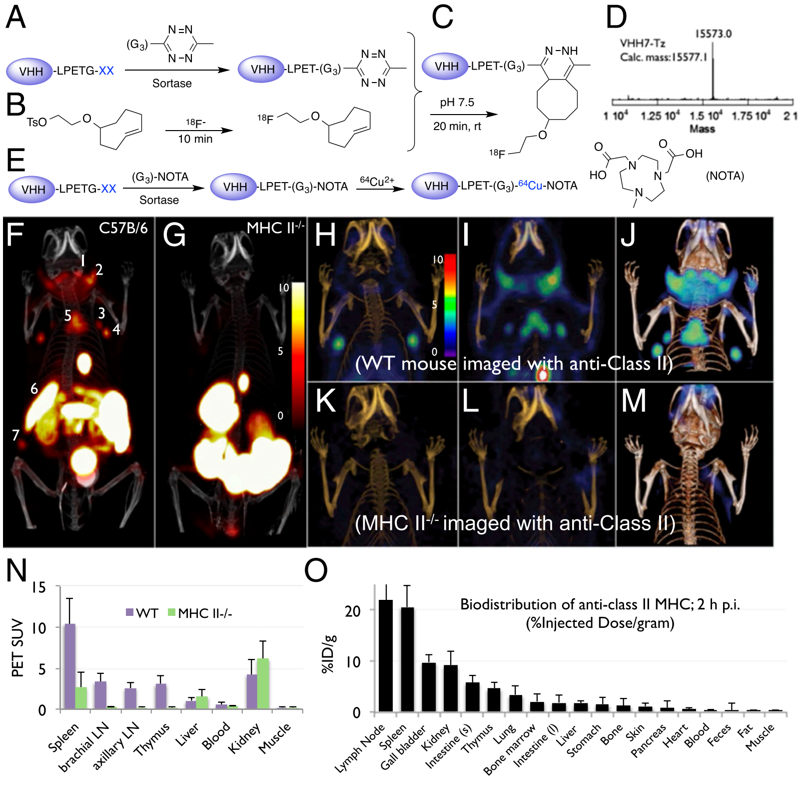

Fig. 2. (*A*–*E*) Site-specific ^{18}F or ^{64}Cu labeling of single-domain antibodies (VHHs) using sortase. (*A*) A single-domain antibody fragment (VHH), equipped at its C terminus with the LPXTG sortase recognition motif followed by a His tag, is incubated with sortase A, which cleaves the threonine–glycine bond to yield the reactive thioacyl intermediate. Addition of a peptide with N-terminal glycine residues and a functional moiety of choice enables site-specific modification of the VHH. We thus modified a VHH with a (Gly)$_3$-tetrazine (Tz), as confirmed by LC-MS (liquid chromatography-mass spectrometry) (*D*, VHH7-Tz). (*B*) A tosyl-TCO and ^{18}F-K222/K_2CO_3 were combined to produce ^{18}F-TCO. (*C*) ^{18}F-TCO was added to the Tz-modified VHH, and, after ∼20 min, the labeled VHH was retrieved by rapid size-exclusion chromatography. (*E*) The sortase reaction was used to install a NOTA functionality at the C terminus of a VHH followed by addition of $^{64}Cu^{2+}$ to produce ^{64}Cu-VHH. (*F*–*M*) ^{18}F-VHH7 (anti-mouse class II MHC) detects secondary lymphoid organs. (*F* and *G*) PET-CT images of class II MHC$^{-/-}$ (*G*) and C57BL/6 (*F*) mice 2 h postinjection of ^{18}F-VHH7; numbers indicate (*i*) lymph nodes (numbers 1, 2, 3, 4, and 7), (*ii*) thymus (number 5), and (*iii*) spleen (number 6). (*H* and *I*) Coronal PET-CT images of C57BL/6 mouse imaged with ^{18}F-VHH7, moving from anterior to posterior. In *H* and *I*, different sets of lymph nodes and thymus are visible. (*K* and *L*) Coronal PET-CT images of an MHC-II$^{-/-}$ mouse imaged with ^{18}F-VHH7, moving from anterior to posterior. In neither *K* nor *L*, lymph nodes or thymus is visible. (*J* and *M*) PET-CT as maximum intensity projections of all slices for a C57BL/6 and a class II MHC$^{-/-}$ mouse 2 h postinjection of ^{18}F-VHH7. In green, accumulation of ^{18}F-VHH7 in lymph nodes and thymus. (PET scale bars have arbitrary units.) See Movies S1*A*, S1*B*, S2*A*, and S2*B* for 3D visualization of secondary lymphoid organs. (*N* and *O*) PET signals in vivo and postmortem biodistribution in all organs.

positive for VHH7 and DC13 (Fig. 3 *H* and *I*). Postmortem histology of the tumor further verified the presence of inflammatory cells in/around the tumor, with clearly visible infiltrating macrophages and neutrophils (Fig. 3*L*). We have thus demonstrated noninvasive imaging of class II MHC$^+$ cells and CD11b$^+$ cells, both in normal and in tumor-bearing mice.

^{18}F-VHH7 Detects Class II MHC$^+$ Cells Associated with Small Tumors at Early Stages. Is it possible to image small tumors also at earlier stages of growth? To address this question, we imaged NOD/SCID mice xenografted with 5×10^6 Mel-Juso human melanoma cells at 6 d, 20 d, and 27 d postinjection. We detected inflammation at the site of the malignant growth at the earliest time point after injection, a time when the incipient tumors are neither visible nor detectable by palpation (Fig. 3*E*). FACS analysis on cell suspensions prepared from the excised tumors again confirmed the presence of tumor-infiltrating class II MHC$^+$ cells (Fig. 3*H*). It may thus be worthwhile to explore early-stage detection of diseases characterized by an inflammatory signature, such as multiple sclerosis, diabetes, or infections (5).

The longer half-life of ^{64}Cu (12.7 h) relative to ^{18}F (110 min) in principle allows a more extended imaging period to establish tissue penetration and dwell time of VHHs on their targets. We developed a NOTA-(Gly)$_3$ sortase nucleophile to enable site-specific labeling of VHHs (Fig. 2*D* and Fig. S3) via this high-affinity copper-chelating agent (K_{eq} for Cu^{2+} of ~10^{21}) (32). The [Cu^{2+}-NOTA] complex is kinetically inert, with minimal metal exchange when exposed to other metals present in body (33). We produced site-specifically labeled [(^{64}Cu)-NOTA]-VHHs in high radiochemical yield (~90% decay corrected) and used ^{64}Cu-VHH7 to image a C57BL/6 WT mouse at 4 h, 8 h, and 24 h postinjection. VHH7 stayed on its target (secondary lymphoid organs) even after 24 h (Fig. S4) but produced images with an inferior signal-to-noise ratio compared with ^{18}F-VHH7 (compare Fig. 2 with Fig. S4).

^{18}F-VHH7 and ^{18}F-VHHDC13 Detect Infiltration of Immune Cells in B16 Melanoma Tumor-Bearing Mice in a Syngeneic Setting. Next, we explored B16 melanoma-bearing mice and found that here, too, we could readily image the presence of the primary tumor via the presence of CD11b$^+$ and class II MHC$^+$ cells, without a need for melanoma-specific markers (Fig. 4 *A* and *B* and Movies S5*A*, S5*B*, S5*C*, S6*A*, and S6*B*). We also performed imaging experiments on B16 melanoma-bearing mice using ^{18}F-2-fluorodeoxyglucose (^{18}F-FDG), a standard means of staging tumor patients by PET. ^{18}F-FDG revealed the presence of the tumor but produced images of inferior specificity compared with the use of ^{18}F-VHHs (Fig. 4*C* and Movie S7).

Successful Detection of Infiltrated Myeloid Cells Using ^{18}F-Labeled VHHDC13 upon Injection of Complete Freund's Adjuvant. Finally we examined inflammation in response to administration of complete Freund's adjuvant (CFA). Administration of CFA leads to the influx and accumulation of myeloid cells at the site of the injection and draining lymph nodes within 24 h. When we injected animals with CFA into the left front paw and imaged them 24 h later with ^{18}F- or ^{64}Cu-labeled VHH7, inflammation was readily apparent, with VHHDC13 showing a stronger signal than VHH7 in the inflamed region (Fig. 4 *D* and *E*, and Movies S8*A*, S8*B*, S9, S10, and S11). ^{18}F-2-fluorodeoxyglucose (FDG) was used for comparison and failed to detect inflammation evoked by CFA (Fig. 4*F* and Movies S12*A*, S12*B*, and S12*C*). Accumulation of ^{18}F-VHHDC13 is consistent with the massive influx of CD11b$^+$ neutrophils generally observed at the site of injection 24 h after administration of CFA.

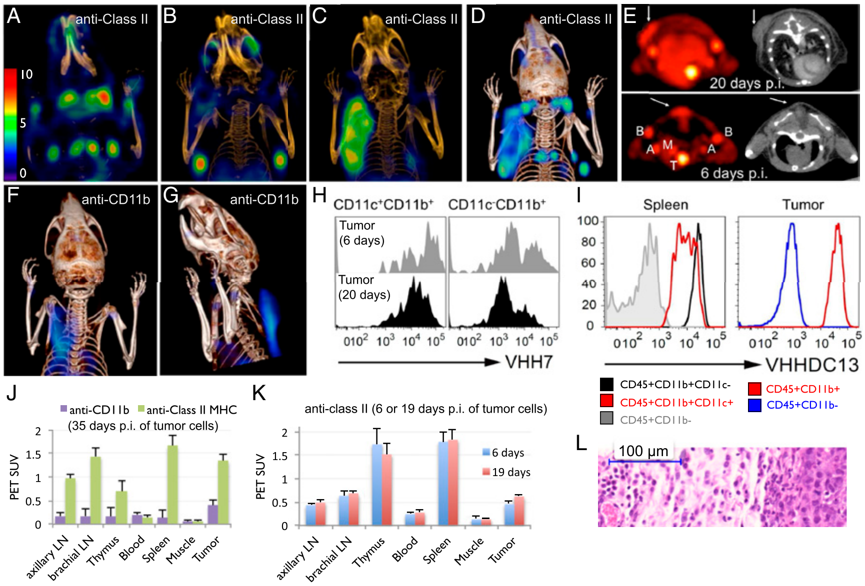

Fig. 3. ^{18}F-VHH7 (anti-mouse class II MHC) and ^{18}F-VHHDC13 (anti-mouse CD11b) detects inflammation. Tumor-associated class II MHC$^+$ cells were visualized using ^{18}F-VHH7. A NOD-SCID mouse was inoculated subcutaneously on the back of the left shoulder with 5×10^6 human Mel-Juso melanoma cells and imaged 35 days postinjection. (*A*–*C*) Coronal PET-CT images, moving from anterior to posterior. In *A* and *B*, different sets of lymph nodes are visible. In *C*, tumor-associated class II MHC$^+$ cells are visible, attributable to influx of host-derived class II MHC$^+$ cells. (*D*) PET-CT as maximum intensity projections of all slices. See Movie S3 for a 3D visualization of lymph nodes and tumor-associated class II MHC$^+$ cells. (*E*) ^{18}F-VHH7 detects class II MHC$^+$ cells associated with small tumors at early stages. NOD-SCID mice were inoculated with Mel-Juso cells as in *A*, 20 d (*Upper*) and 6 d (*Lower*) prior to imaging. Transverse PET and CT images (*Left* and *Right*, respectively) are shown for better visualization of the class II MHC$^+$ cells at the site of cancer cells. Images are all window-leveled to the same intensity. Tumors and associated class II MHC$^+$ cells are highlighted with arrows. Axillary (label A), brachial (label B), and mediastinal (label M) lymph nodes and thymus (label T) are shown in *E*, *Lower*. (*F* and *G*) A NOD-SCID mouse was inoculated subcutaneously on the back of the left shoulder with 5×10^6 human Mel-Juso melanoma cells and imaged 35 days postinjection with ^{18}F-VHHDC13. Tumor-associated CD11b$^+$ cells are visible, attributable to influx of host-derived CD11b$^+$ cells. See Movie S4 for a 3D visualization. (*H* and *I*) FACS analysis of tumor-infiltrating immune cells. The next day, tumors were excised and digested with collagenase D, and tumor-infiltrating cells were obtained after Percoll gradient. Cell suspensions were then stained for FACS analysis. (*H*) Histograms show the FACS staining of mouse CD45$^+$ tumor-infiltrating cells with VHH7-Alexa 647. Histograms on the *Left* are gated on CD11c$^+$CD11b$^+$ cells (dendritic cells), and histograms on the *Right* are gated on CD11c$^-$CD11b$^+$cells (macrophages and other myeloid cells) for the indicated time points. (*I*) Tumor-infiltrating cells were harvested 35 d after tumor inoculation as in *H* and stained with VHHDC13-Alexa 647. Histograms show the levels of CD11b as measured by VHHDC13 on the indicated cell populations. Spleen from the same mouse is shown for comparison. Histograms are representative of two to four mice with similar results. (*J*) PET signals in vivo for the indicated experiment in *D* and *F*. (*K*) PET signals in vivo for the indicated experiment in *E*. (*L*) Hematoxylin/eosin (H&E) stains of the tumor from the mice in the part *D* (human melanoma tumor in NOD-SCID mouse; 35 d postinjection of the cells).

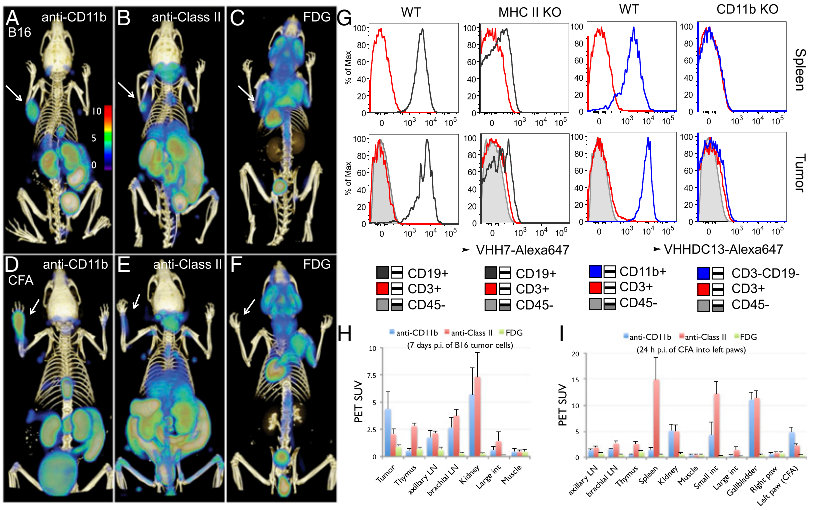

Fig. 4. ^{18}F-VHH7 (anti-mouse class II MHC) and ^{18}F-VHHDC13 (anti-mouse CD11b) detects inflammation. (*A*–*C*) Tumor-associated CD11b$^+$ and class II MHC$^+$ cells were visualized using ^{18}F-VHHDC13 and VHH7, with ^{18}F-FDG failing to yield a strong tumor-specific signal. Mice were inoculated subcutaneously on the back of the left shoulder with 1 × 10^6 B16 melanoma cells and imaged 7 d postinjection. See Movies S9, S10, and S11 for a 3D visualization. (*A*) ^{18}F-VHHDC13 was injected 90 min prior to imaging. The tumor on the left shoulder is clearly visible, attributable to the influx of CD11b$^+$ cells. (*B*) ^{18}F-VHH7 was injected 90 min prior to imaging. The lymph nodes and the tumor on the left shoulder are visible, attributable to the influx of class II MHC$^+$ cells; detection of influx of CD11b$^+$ cells is superior to the detection of influx of class II MHC$^+$ cells. (*C*) ^{18}F-FDG was injected 90 min prior to imaging. The tumor could be visualized via ^{18}F-FDG with lower specificity compared with VHHs specifically relative to anti-CD11b. (*D*–*F*) Complete Freund's adjuvant (CFA) was injected into the left paw of C57BL/6 mice, and ^{18}F-VHHDC13 (*D*), ^{18}F-VHH7 (*E*), or ^{18}F-FDG (*F*) was used 24 h after CFA injection. PET-CT images were obtained 1.5 h postinjection of ^{18}F agents. Images are all window-leveled to the same intensity for comparison. See Movies S5*A*, S5*B*, S5*C*, S6*A*, S6*B*, S7, S8*A*, and S8*B* for a 3D visualization. (PET scale bars have arbitrary units.) (*G*) WT or the indicated KO mice were injected subcutaneously with 8 × 10^5 B16 melanoma cells, and 8 days later injected i.v. with 20 μg of the indicated VHH conjugated to Alexa 647. After 90 min of VHH injection, animals were sacrificed, spleen and tumor were excised, and single-cell suspensions were further stained with anti-CD3, anti-CD19, anti-CD11b, and anti-CD45 for FACS analysis. Histograms are representative of two to four mice with similar results. (*H*) PET signals in vivo for the indicated experiments in *A*–*C*. (*I*) PET signals in vivo for the indicated experiments in *D*–*F*.

Discussion

Using a combination of single domain antibodies (VHHs), we showed that it is possible to track immune responses with excellent specificity. CD11b$^+$ or class II MHC$^+$ cells can serve as sentinels to detect the presence of the cancerous tissue they surround or invade. Although class II MHC and CD11b are expressed on many activated myeloid cells, such as macrophages and dendritic cells, the observed signal strength for imaging may vary with the extent of activation, and not all tumors may recruit myeloid cells equally efficiently. The approach described here obviates the need for the generation of panels of tumor-specific antibodies, if indeed such accumulation of myeloid cells is a general phenomenon, as suggested by the available evidence (2, 34). With the availability of anti-human VHHs, the ability to monitor the presence or absence of neutrophils and activated macrophages as an indicator of inflammation should be transposable to a clinical setting as a diagnostic tool. The potential immunogenicity of VHHs may limit their therapeutic use, especially when repeated administration would be required, but approaches to humanize VHHs have been described (12). VHH-based PET will likely complement the information provided by ^{18}F-FDG PET. The metabolic status of tumors can be assessed using ^{18}F-FDG PET in ways that VHH-PET or other forms of immuno-PET cannot. In contrast, VHH-PET can in principle reveal the occurrence and extent of an immune response and do so noninvasively. The combination of ^{18}F-FDG-PET and VHH-PET may provide valuable additional information on various forms of therapy. An interesting possibility is the development of single-domain antibodies capable of recognizing markers on T cells with distinct functional properties, including exhausted T cells, for example, by the presence of PD-1, and the presence of PD-L1 on tumors. Given the recent successes in the application of antibodies that target immunological checkpoints, there is an urgent need to monitor the progress of such immunotherapies. The advantages of the small size of VHHs in conjunction with PET-compatible isotopes, such as ^{18}F, should enable further refinement of immuno-PET in a clinical setting. Although the present results are geared toward the detection of neutrophils and antigen-presenting cells, an important future goal will be to extend this approach to T cell-specific markers.

Materials and Methods

Synthesis of $(Gly)_3$-Tetrazine.

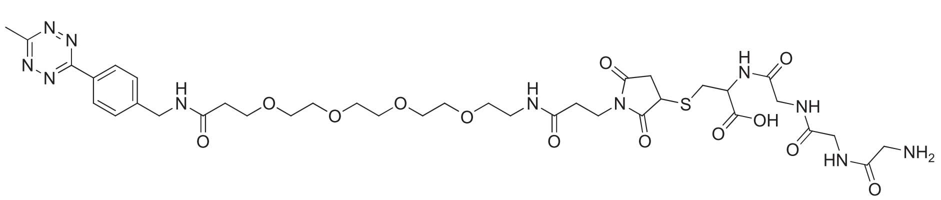

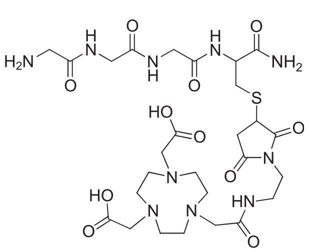

The tetrapeptide GGGC was synthesized by standard solid-phase peptide synthesis. Maleimide-tetrazine (ClickChemistryTools) was dissolved in 0.1 M phosphate buffer (PB), pH 7. The tetrapeptide GGGC was added and left to stir at room temperature for 3 h until TLC (1:1 Hex:EtOAc vol/vol) indicated near-complete conversion to the product. The solution was filtered and purified by reverse-phase HPLC with a semipreparative column (C_{18} column, Gemini, 5 μm, 10 × 250 mm; Phenomenex) at a flow rate of 5.0 mL/min: solvent A, 0.1% TFA in H_2O; solvent B, 0.1% TFA in CH_3CN. $(G)_3$-Tetrazine eluted at 30–35% (vol/vol) solvent B. Fractions containing pure product were collected and lyophilized. LC-MS calculated for $C_{37}H_{54}N_{11}O_{13}S[M+H]^+$ was 892.362, found 892.370.

Synthesis of $(Gly)_3$-NOTA. Maleimide-NOTA (Macromolecules) was dissolved in 0.1 M PB, pH 7. The tetrapeptide GGGC was added at room temperature for 3 h until TLC (1:1 Hex:EtOAc vol/vol) indicated almost complete conversion to the product. The solution was purified by RP-HPLC on a semipreparative column (C_{18} column, Gemini, 5 μm, 10 × 250 mm; Phenomenex) at a flow rate of 5.0 mL/min: solvent A, 0.1% TFA in H_2O; solvent B, 0.1% TFA in CH_3CN. The desired product eluted from 15% to 20% (vol/vol) solvent B. Fractions containing pure product were collected and lyophilized. LC-MS calculated for $C_{27}H_{45}N_{10}O_{11}S$ $[M+H]^+$ was 717.298, found 717.305.

Enzymatic Incorporation of Substrates into Proteins Using Sortase. The pentamutant sortase A, with an improved k_{cat}, was used (35). Reaction mixtures (1 mL) contained Tris·HCl (50 mM, pH 7.5), $CaCl_2$ (10 mM), NaCl (150 mM), triglycine-containing probe (500 μM), LPETG-containing probe (100 μM), and sortase (5 μM) (11, 36). After incubation at 4 °C with agitation for 2 h, reaction products were analyzed by LC-MS, with yields generally >90%. When the yield was below 90%, the reaction was allowed to proceed for an additional 2 h, with addition of sortase to 10 μM and triglycine-containing probe to 750 μM. Ni-NTA beads were added to the reaction mixture with agitation for 5 min at 25 °C, followed by centrifugation to remove sortase and any remaining unreacted His-tagged substrate. The final product—either the tetrazine-labeled protein, NOTA-labeled protein, or fluorophore-labeled protein—was purified by size-exclusion chromatography in PBS or Tris·HCl (50 mM, pH 7.5). The labeled protein was stored at −20 °C with 5% (vol/vol) glycerol and was stable for up to 3 mo.

Synthesis and Characterization of ^{18}F-VHHs. In a typical reaction, a 1.5-mL centrifuge tube was loaded with VHH7-Tz in 1× PBS (40 μL, 150 μM), 1× PBS (300 μL), and ^{18}F-TCO in DMSO [4.0 mCi (148.0 MBq), 100 μL]. The tube was sealed and shaken at room temperature for 20 min. The mixture was analyzed by radio-TLC [instant thin layer chromatography (ITLC), 100% MeCN, R_f ^{18}F-TCO = 0.9, R_f ^{18}F-VHH7 = 0.0] showing 90% conversion to ^{18}F-VHH7. The reaction mixture was loaded onto a PD-10 size-exclusion cartridge (GE Healthcare), and elution with 1× PBS provided 2.3 mCi (85.1 MBq) of ^{18}F-VHH7 in 75.8% decay-corrected radiochemical yield. Starting with 5.3 mCi (196.1 MBq) ^{18}F-TCO, ^{18}F-VHHDC13 was prepared following the same procedure as described for ^{18}F-VHH7 to give 2.8 mCi (103.6 MBq) after size-exclusion chromatography, a 69.7% decay-corrected radiochemical yield.

Synthesis and Characterization of ^{64}Cu-VHHs. In a typical reaction, a 1.5-mL centrifuge tube was loaded with VHH7-NOTA [400 μL, 20 μM in 200 mM NH_4OAc buffer (pH 6.5)] and $^{64}CuCl_2$ (5.7 mCi, 210.8 MBq) in 200 mM NH_4OAc buffer (75 μL, pH 6.5). The tube was sealed and shaken at 37 °C for 20 min. The mixture was analyzed by radio-TLC (ITLC, 50 mM EDTA, pH 7, R_f ^{64}Cu/EDTA = 1.0, R_f ^{64}Cu-VHH7 = 0.0) showing 98% conversion to ^{64}Cu-VHH7. At this time, the mixture was loaded onto a PD-10 size-exclusion cartridge, and elution with 1× PBS provided 5.2 mCi (192.4 MBq) of ^{64}Cu-VHH7 in 94.2% decay-corrected radiochemical yield. Starting with 3.5 mCi (129.5 MBq) $^{64}CuCl_2$, ^{64}Cu-VHHDC13 was prepared following the same procedure as described for ^{64}Cu-VHH7 to give 3.1 mCi (114.7 MBq) after size-exclusion chromatography, a 92.3% decay-corrected radiochemical yield. Before injection, both ^{64}Cu-VHH7 and ^{64}Cu-VHHDC13 were analyzed by radio-TLC (ITLC, 50 mM EDTA, pH 7, R_f ^{64}Cu/EDTA = 1.0, R_f ^{64}Cu-VHH7 and ^{64}Cu-VHHDC13 = 0.0) and were found to have 99.6% and 99.8% radiochemical purity, respectively.

PET-CT Imaging. All procedures and animal protocols were approved by the Massachusetts General Hospital subcommittee on research animal care.

ACKNOWLEDGMENTS. M.R. is a Cancer Research Institute Irvington Fellow supported by the Cancer Research Institute, and J.N.D. is a Calouste Gulbenkian Scholar funded by the Calouste Gulbenkian Foundation, Champalimaud Foundation, Portuguese Science and Technology Foundation, and Portuguese Ministry of Health. This work was funded by NIH R01-AI087879-06 (to H.L.P.), DP1-GM106409-03 (an NIH Pioneer Award to H.L.P.), R01-GM100518-04 (to H.L.P.), and by the Lustgarten Foundation (H.L.P.).

1. Forssell J, et al. (2007) High macrophage infiltration along the tumor front correlates with improved survival in colon cancer. *Clin Cancer Res* 13(5):1472–1479.
2. DeNardo DG, Andreu P, Coussens LM (2010) Interactions between lymphocytes and myeloid cells regulate pro- versus anti-tumor immunity. *Cancer Metastasis Rev* 29(2):309–316.
3. Allavena P, Sica A, Solinas G, Porta C, Mantovani A (2008) The inflammatory microenvironment in tumor progression: The role of tumor-associated macrophages. *Crit Rev Oncol Hematol* 66(1):1–9.
4. Mosser DM (2003) The many faces of macrophage activation. *J Leukoc Biol* 73(2):209–212.
5. Wu C, Li F, Niu G, Chen X (2013) PET imaging of inflammation biomarkers. *Theranostics* 3(7):448–466.
6. Hackel BJ, Kimura RH, Gambhir SS (2012) Use of (64)Cu-labeled fibronectin domain with EGFR-overexpressing tumor xenograft: Molecular imaging. *Radiology* 263(1):179–188.
7. Liu Z, et al. (2012) 99mTc-labeled RGD-BBN peptide for small-animal SPECT/CT of lung carcinoma. *Mol Pharm* 9(5):1409–1417.
8. Smolarek D, Bertrand O, Czerwinski M (2012) Variable fragments of heavy chain antibodies (VHHs): A new magic bullet molecule of medicine? *Postepy Hig Med Dosw (Online)* 66:348–358.
9. Holliger P, Prospero T, Winter G (1993) "Diabodies": Small bivalent and bispecific antibody fragments. *Proc Natl Acad Sci USA* 90(14):6444–6448.
10. Pardon E, et al. (2014) A general protocol for the generation of Nanobodies for structural biology. *Nat Protoc* 9(3):674–693.
11. Witte MD, et al. (2012) Preparation of unnatural N-to-N and C-to-C protein fusions. *Proc Natl Acad Sci USA* 109(30):11993–11998.
12. Vincke C, et al. (2009) General strategy to humanize a camelid single-domain antibody and identification of a universal humanized nanobody scaffold. *J Biol Chem* 284(5):3273–3284.
13. De Meyer T, Muyldermans S, Depicker A (2014) Nanobody-based products as research and diagnostic tools. *Trends Biotechnol* 32(5):263–270.
14. Guimaraes CP, et al. (2013) Site-specific C-terminal and internal loop labeling of proteins using sortase-mediated reactions. *Nat Protoc* 8(9):1787–1799.
15. Boes M., et al. (2002) T-cell engagement of dendritic cells rapidly rearranges MHC class II transport. *Nature* 418, 983–988.
16. Grusby MJ, Johnson RS, Papaioannou VE, Glimcher LH (1991) Depletion of CD4+ T cells in major histocompatibility complex class II-deficient mice. *Science* 253(5026):1417–1420.
17. Tanaka K, Fukase K (2008) PET (positron emission tomography) imaging of biomolecules using metal-DOTA complexes: A new collaborative challenge by chemists, biologists, and physicians for future diagnostics and exploration of in vivo dynamics. *Org Biomol Chem* 6(5):815–828.
18. Fani M, André JP, Maecke HR (2008) 68Ga-PET: A powerful generator-based alternative to cyclotron-based PET radiopharmaceuticals. *Contrast Media Mol Imaging* 3(2):67–77.
19. Vosjan MJWD, et al. (2010) Conjugation and radiolabeling of monoclonal antibodies with zirconium-89 for PET imaging using the bifunctional chelate p-isothiocyanatobenzyl-desferrioxamine. *Nat Protoc* 5(4):739–743.
20. Furuya T, Kuttruff CA, Ritter T (2008) Carbon-fluorine bond formation. *Curr Opin Drug Discov Devel* 11(6):803–819.
21. Truong T, Klimovica K, Daugulis O (2013) Copper-catalyzed, directing group-assisted fluorination of arene and heteroarene C-H bonds. *J Am Chem Soc* 135(25):9342–9345.
22. Bohnen NI, Djang DSW, Herholz K, Anzai Y, Minoshima S (2012) Effectiveness and safety of 18F-FDG PET in the evaluation of dementia: A review of the recent literature. *J Nucl Med* 53(1):59–71.
23. Groheux D, et al. (2011) Correlation of high 18F-FDG uptake to clinical, pathological and biological prognostic factors in breast cancer. *Eur J Nucl Med Mol Imaging* 38(3):426–435.
24. Youssef G, et al. (2012) The use of 18F-FDG PET in the diagnosis of cardiac sarcoidosis: A systematic review and metaanalysis including the Ontario experience. *J Nucl Med* 53(2):241–248.
25. Waldherr C, et al. (2005) Monitoring antiproliferative responses to kinase inhibitor therapy in mice with 3′-deoxy-3′-18F-fluorothymidine PET. *J Nucl Med* 46(1):114–120.
26. Tavaré R, et al. (2014) Engineered antibody fragments for immuno-PET imaging of endogenous CD8+ T cells in vivo. *Proc Natl Acad Sci USA* 111(3):1108–1113.
27. Blackman ML, Royzen M, Fox JM (2008) Tetrazine ligation: Fast bioconjugation based on inverse-electron-demand Diels-Alder reactivity. *J Am Chem Soc* 130(41):13518–13519.
28. Karver MR, Weissleder R, Hilderbrand SA (2011) Synthesis and evaluation of a series of 1,2,4,5-tetrazines for bioorthogonal conjugation. *Bioconjug Chem* 22(11):2263–2270.
29. Karver MR, Weissleder R, Hilderbrand SA (2012) Bioorthogonal reaction pairs enable simultaneous, selective, multi-target imaging. *Angew Chem Int Ed Engl* 51(4):920–922.
30. Keliher EJ, Reiner T, Turetsky A, Hilderbrand SA, Weissleder R (2011) High-yielding, two-step 18F labeling strategy for 18F-PARP1 inhibitors. *ChemMedChem* 6(3):424–427.
31. Robila V, et al. (2008) MHC class II presentation of gp100 epitopes in melanoma cells requires the function of conventional endosomes and is influenced by melanosomes. *J Immunol 1950* 181(11):7843–7852.
32. Delgado R, Sun Y, Motekaitis RJ, Martell AE (1993) Stabilities of divalent and trivalent metal ion complexes of macrocyclic triazatriacetic acids. *Inorg Chem* 32(15):3320–3326.
33. Zhang Y, et al. (2011) Positron emission tomography imaging of CD105 expression with a 64Cu-labeled monoclonal antibody: NOTA is superior to DOTA. *PLoS ONE* 6(12):e28005.
34. Coussens LM, Zitvogel L, Palucka AK (2013) Neutralizing tumor-promoting chronic inflammation: A magic bullet? *Science* 339(6117):286–291.
35. Chen I, Dorr BM, Liu DR (2011) A general strategy for the evolution of bond-forming enzymes using yeast display. *Proc Natl Acad Sci USA* 108(28):11399–11404.
36. Theile CS, et al. (2013) Site-specific N-terminal labeling of proteins using sortase-mediated reactions. *Nat Protoc* 8(9):1800–1807.